EPJ manuscript No.
(will be inserted by the editor)

Soft hadron production in pp interactions up to ISR energies

H. Müller

Institut für Kern- und Hadronenphysik, Forschungszentrum Rossendorf, Postfach 510119, 01314 Dresden, Germany

Received: date / Revised version: date

Abstract. Soft hadron production is described as a two-step process, where the interaction of the partonic constituents of the colliding hadrons leads to the production of intermediate subsystems (fireballs), which decay subsequently into hadrons. The weights of the various final states are derived from the corresponding phase-space factors modified by empirical transition elements. The results compare well with data at energies between particle production thresholds and ISR energies. Special emphasis is put on correlation data, which offer the opportunity to shed some light on the question whether particle production proceeds via fireballs or strings.

1 Introduction

QCD is assumed to be the theory of the strong interaction. Soft hadron production, however, is a nonperturbative process which at present cannot be calculated by QCD. Thus, the understanding of soft hadron production is still based on phenomenological approaches like, *e.g.*, the dual parton (DPM) [1], the VENUS [2] or the PYTHIA-LUND [3,4,5,6] models. Within these approaches hadrons are considered as composite objects consisting of partons (quarks and gluons) the interaction of which is assumed to proceed in two steps. In a first step excited subsystems, usually called strings, are produced which decay afterwards into stable particles and resonances.

Ingredients of these models are structure functions, parton-parton cross sections and fragmentation functions. The structure functions of the interacting hadrons contain the information about the momentum distribution of partons. From the cross sections for parton-parton interactions the number of strings produced in a single hadron-hadron scattering can be deduced, and fragmentation functions describe the decay of strings into hadrons. These approaches make maximal use of the information available from lepton-hadron and lepton-lepton interactions as well as from general properties of the scattering amplitude like unitarity and analyticity.

On the other hand the first attempts to understand multiple hadron production in hadronic interactions were based on statistical considerations and the observation of excited intermediate subsystems called fireballs (FB) (see the reviews [7,8,9]). A modern version of a thermodynamical approach can be found, *e.g.*, in ref. [10].

The Rossendorf collision (ROC) model [11,12,13,14, 15,16,17] is basically a statistical approach in deriving the relative contributions of the various final channels by calculating their statistical weights from the phase-space factors, which are, however, strongly modified by empirical transition matrix elements. It aims at describing soft hadron production in the energy region between particle production thresholds and ISR energies. For this purpose the basic ingredients of hadron production models are reformulated in such a way that they are applicable at low energies as well. The ROC model is built as a minimal approach in the sense that the number of parameters is restricted to the minimum necessary to well reproduce the main features of the available data. Special emphasis is put on the consideration of short-range correlations, because the FB concept yields a natural explanation of the observed phenomena.

The present paper is organized as follows. In sect. 2 the basic features of the ROC model are explained. Section 3 contains a comparison of selected experimental data with model calculations. In order to show differences between string and FB approaches with regard to correlation data the ROC model is contrasted with the PYTHIA-LUND model [6]. By means of a special version of the ROC model, where FBs are degenerated into single hadrons, the importance of FBs for the description of correlation data is demonstrated. Conclusions are summarized in sect. 4.

2 The model

The basic idea of a statistical approach consists in the assumption that the probabilities of formation of the various final states are proportional to their statistical weights. This idea was implemented by Fermi [18] fifty years ago, but his model turned out to be applicable only at relatively low energies. At higher energies it is no longer a good approximation to assume that the whole initial energy is randomly distributed among the final particles. Particles with high transverse momentum, *e.g.*, are produced with extremely low probability indicating that the final states are dynamically linked with the initial state.

In contrast to this early attempt the ROC model is based on the following modified statistical approach. Instead of calculating the statistical weights from the whole phase-space the dynamics of the interaction is implemented in form of empirical functions which either suppress certain regions of the phase-space or impose additional non-statistical weights. We define a channel α by the number n, masses m_i and quantum numbers of the final particles. The relative probability of populating a channel α is calculated as the product of the Lorentz-invariant phase-space factor $\mathrm{d}L_n(s;\alpha)$ with the square of an empirical matrix element A^2, which describes the dynamics of the interaction process. Here, $s = p^2$ denotes the square of the total energy with p being the total four-momentum. The phase-space factor is defined as the integral over the momenta of the final particles with energy and momentum conservation taken into account,

$$\mathrm{d}L_n(s;\alpha) = \mathrm{d}L_n(s;m_1,\ldots,m_n) = \prod_{i=1}^{n} \frac{\mathrm{d}^3 p_i}{2e_i}\,\delta^4(p-\sum_{i=1}^{n} p_i), \tag{1}$$

where the four-momentum of the i-th particle is denoted by $p_i = (e_i, \mathbf{p}_i)$ with $p_i^2 = m_i^2$. For numerical calculations the δ function in eq. (1) is removed by introducing a new set of $3n-4$ variables to replace the $3n$ three-momentum components. It is reasonable to choose a set of variables, which reflects the underlying physical picture of the interaction process. In fig. 1 the reaction

$$a + b \to FB_1 + \ldots + FB_N \to h_1 + \ldots + h_n$$

between hadrons a and b resulting in the production of n particles is schematically depicted. First, $2 \le N \le n$ intermediate particle groups called FBs are produced, which decay into so-called primary particles. The primary particles define the channels for which the weights (3) are calculated. Among them are resonances, which decay subsequently into stable hadrons. The phase-space factor corresponding to the diagram of fig. 1 can be calculated according to ref. [19]

$$\mathrm{d}L_n\,(s;\boldsymbol{\alpha}_N) = \left[\prod_{I=1}^{N} \mathrm{d}M_I^2 L_{n_I}(M_I;\alpha_I)\right] \mathrm{d}L_N(s;M_1,\ldots,M_N) \tag{2}$$

with the invariant masses of the FBs equal to $M_I = \sqrt{P_I^2} = \sqrt{\left(\sum_{i=1}^{n_I} p_i\right)^2}$ and the final channel defined as the vector $\boldsymbol{\alpha}_N = (\alpha_1,\ldots,\alpha_N)$ of the decay channels of the individual FBs. The probability of populating the channel $\boldsymbol{\alpha}_N$ is given by

$$\mathrm{d}W(s;\boldsymbol{\alpha}_N) \propto \mathrm{d}L_n(s;\boldsymbol{\alpha}_N)\,A^2\,. \tag{3}$$

Here, the square of the matrix element A^2 contains the dynamical input and is split into factors

$$A^2 = A_{\mathrm{i}}^2 A_{\mathrm{qs}}^2 A_{\mathrm{ex}}^2 A_{\mathrm{t}}^2 A_{\mathrm{l}}^2 A_{\mathrm{st}}^2\,,$$

which describe the interaction A_{i}^2 resulting in the production of N FBs, the production of hadrons A_{qs}^2 via the creation of quark-anti-quark ($q\bar{q}$) pairs , the invariant-mass distribution of the FBs A_{ex}^2, the transverse A_{t}^2 and longitudinal A_{l}^2 momentum distribution of the FBs, and, finally, some additional factors A_{st}^2 necessary for the calculation of the statistical weights. In the following subsections these factors will be discussed in more detail.

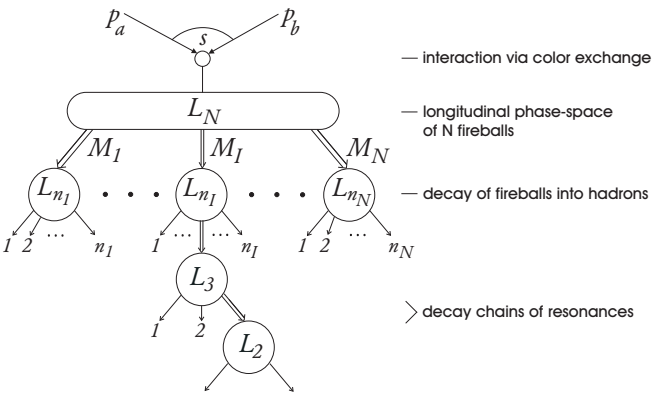

Fig. 1. Phase-space decomposition of a two-step process. N FBs with masses $M_I (I = 1 \ldots N)$ are produced in the interaction of two hadrons a and b with four-momenta p_a and p_b. The FBs decay in the second step, where the I-th FB disintegrates into n_I primary particles with $\sum_{I=1}^{N} n_I = n$. Resonances among the primary particles decay afterwards into stable hadrons. A possible decay chain is shown.

2.1 The interaction A_{i}^2

In models like DPM [1] or VENUS [2] the colliding hadrons are considered as extended and composite objects consisting of an indefinite number of partons, the interaction of which is assumed to proceed via color exchange. If, *e.g.*, the color exchange between the valence quarks of two baryons takes place, then two strings are produced. Each of them consists of the remaining diquark and the valence quark removed from the other baryon. Since more complicated exchanges are possible and the collision may proceed at different impact parameters a varying number of strings is produced. The corresponding probabilities are derived from Gribov-Regge theory [20] in the limit of high energies in combination with the use of profile functions for integrating over the impact parameter. PYTHIA [6] describes low-p_{t} events on the basis of the multiple interaction model of ref. [5], which extends a high-p_{t} picture down into the low-p_{t} region by regularizing the p_{t} scale. The number of (independent) parton-parton collisions in one event depends on the impact parameter and on the assumed matter distribution inside the interacting hadrons.

In the ROC model, non-statistical weights $A_{\mathrm{i}}^2(N)$ for producing a definite number N of FBs are introduced. This is a phenomenological parameterization of the contributions from the different color exchange diagrams and of the integral over the impact parameter, which we apply also at low energies. Such a dynamical input is necessary, because the phase-space factor alone tends to overestimate the number of FBs simply due to the fact that the number

of states increases the more FBs are produced. A thermodynamical approach using a chemical potential as the only parameter to regulate the number of FBs turned out to be not flexible enough. Therefore, the negative binomial distribution is applied where we have two free parameters v and q

$$A_{\rm i}^2(N;q,v) = \binom{-v}{N}(-q)^N(1-q)^v. \quad (4)$$

In the calculations we use the mean $\bar{N}$ and the ratio of the variance to the mean $D = \sigma^2/\bar{N}$ as parameters from which $q = (D-1)/D$ and $v = \bar{N}/(D-1)$ follow. By this means, the whole complicated interaction scenario is described by altogether two parameters in conjunction with the corresponding phase-space factors.

2.2 Quark statistics $A_{\rm qs}^2$

The factor $A_{\rm qs}^2$ stands symbolically for the algorithm applied to sample the possible final states. At first the valence quarks of the interacting hadrons are redistributed among the FBs and then the final hadrons are produced via the creation of new $q\bar{q}$ pairs. All internal quantum numbers are conserved automatically by this procedure.

The complicated details of color exchange diagrams and string drawings are replaced by statistical considerations. For describing the interaction process the notion of quark removal is borrowed from ref. [2]. It is assumed that the multiple interaction of the partonic constituents of the incoming hadrons leads to the creation of N FBs. Color exchange between the constituents results in the removal of the involved quarks and gluons from the incoming hadrons. Removed quarks are found in any of the other FBs with equal probability. The remaining partons of the interacting hadrons form the two leading FBs, the scattered partons the $N-2$ central FBs. In a next step $q\bar{q}$ pairs are produced and randomly (the q's and $\bar{q}$'s independently) distributed between the FBs such that each FB becomes color neutral and contains the minimal number of q's and $\bar{q}$'s necessary for building at least one hadron (meson or baryon). This procedure is the equivalent for the sum over the possible color exchange diagrams with the restriction that the removal of two or three valence quarks or of a single sea quark is neglected. Only the removal of one valence quark with probability $W_{\rm v}$ is considered. The remaining probability $1 - W_{\rm v}$ is understood as gluon or quark-pair removal. As equivalent to string fragmentation each FB is then filled separately with an arbitrary number n_{qI} of additional $q\bar{q}$ pairs where $n_{qI} \geq 0$. Up, down, strange and charm quarks are produced in the ratios

$$u : d : s : c = 1 : 1 : \lambda_{\rm s} : \lambda_{\rm c} \quad (5)$$

with $\lambda_{\rm s}$ and $\lambda_{\rm c}$ being suppression factors due to the heavier masses of the strange and charm quarks. The creation of top quarks can be neglected in the considered energy range.

The final hadrons are built up in each FB independently according to the rules of quark statistics [21] by randomly selecting sequences of q's and $\bar{q}$'s. A $q\bar{q}$ gives a meson, while baryons or antibaryons are formed from qqq or $\bar{q}\bar{q}\bar{q}$. From a given sequence of quarks the different hadrons are formed according to the tables of the particle data group [22]. All baryons marked in the tables with three or four stars, the meson nonets built from u, d and s quarks with angular momenta zero and one ($^1S_0$,$^3S_1$,$^1P_1$,$^3P_0$,$^3P_1$,$^3P_2$) as well as all charmed hadrons are taken into account. An empirical probability distribution

$$W_{\rm h}(m_{\rm h}) \propto \exp\left(-m_{\rm h}/\Theta_{\rm h}\right) \quad (6)$$

with an adjustable parameter $\Theta_{\rm h}$ is used to suppress the formation of the heavier hadrons of mass $m_{\rm h}$. During event generation the current masses of resonances are sampled according to a probability distribution consisting of the product of a relativistic Breit-Wigner distribution, the phase-space factor of the decay products and the above suppression factor $W_h(m_{\rm h})$. The decay of resonances into the various channels proceeds either according to known probabilities or in accordance with the statistical weights of the possible final states in case of unknown decay probabilities.

The described algorithm together with the parameters $\lambda_{\rm s}$, $\lambda_{\rm c}$ and $\Theta_{\rm h}$ is the equivalent of the usually much larger number of parameters describing the fragmentation of strings.

It should be stressed that the ROC model has no parameter fixing the probability of diffractive processes. A diffractive process is usually assumed to proceed via the exchange of a Pomeron, a fictitious particle which does not affect the quantum numbers of the involved particles. In the string models [1,2] diffractive scattering is treated as a special process whose probability is determined by a free parameter adapted to data. In the ROC model diffractive scattering is one of the possible final channels, because there is a certain probability that one or even both leading FBs are identical with the initial protons. This happens if the valence quark content of the considered FB remains unchanged, if no additional $q\bar{q}$ pairs are produced, and if a proton, and not a resonance, is built from the available quarks uud in the recombination phase.

2.3 Mass distribution of FBs $A_{\rm ex}^2$

Until now we have explained how the hadrons forming the final state are sampled. In a next step the integral over the invariant masses of the FBs M_I [see eq. (2)] is performed. Again phase-space alone produces too large FB masses because of their corresponding large numbers of states. To restrict the invariant masses the FBs are assumed to be characterized by a temperature Θ. As matrix element squared the function

$$A_{ex}^2 = \prod_{I=1}^{N}(M_I/\Theta)K_1(M_I/\Theta) \quad (7)$$

with the asymptotic behavior

$$(M_I/\Theta)K_1(M_I/\Theta) \underset{M_I/\Theta\to\infty}{\longrightarrow} \sqrt{M_I/\Theta}\exp(-M_I/\Theta)$$

$$(M_I/\Theta)K_1(M_I/\Theta) \underset{M_I/\Theta\to 0}{\longrightarrow} 1$$

is used. The expression $(M_I/\Theta)K_1(M_I/\Theta)$ is the kernel of the so-called K-transformation (see [19]) used to transform a micro-canonical phase-space distribution depending on the total energy M_I of the I-th FB into a canonical one, which is characterized by a temperature Θ. In eq. (7) K_1 stands for the modified Bessel function. For increasing invariant masses M_I the function $(M_I/\Theta)K_1(M_I/\Theta)$ strongly decreases, while the phase-space factor $L_{n_I}(M_I)$ of the I-th FB becomes larger. Their product has a maximum at a value of M_I determined by the parameter Θ, which thus fixes the average internal excitation energy of the I-th FB. Since FBs consist of only a few particles, we are far from the thermodynamical limit. Therefore, the momenta of the hadrons are calculated from the decay of the FBs according to phase-space and not from macro-canonical distributions.

2.4 Longitudinal phase-space of FBs $A_{\rm t}^2$ and $A_{\rm l}^2$

FBs are proposed to emerge from the interaction of partons, whose momenta inside fast moving hadrons are mainly longitudinal. Due to the finite size of hadrons and the uncertainty principle a small transverse component is present too. This is taken into account by damping large transverse momenta of the FBs using a linear exponential distribution

$$A_{\rm t}^2 = \prod_{I=1}^{N} \exp(-\gamma P_{\rm t,I}) \tag{8}$$

with the mean $\bar{P}_{\rm t} = 2/\gamma$. The parameter γ used here can be directly compared with the analogous parameter employed in string models [1,2]. There, the transverse momenta of the partons, which form the ends of the strings, are restricted, here, we constrain the transverse momenta of the FBs directly.

The longitudinal momentum distribution of the two leading FBs is weighted by

$$A_{\rm l}^2 = (X_1 X_2)^{\beta} \tag{9}$$

with the scaling variables

$$X_1 = (E_1 + P_{\rm z,1})/\sqrt{s} \quad \text{and} \quad X_2 = (E_2 - P_{\rm z,2})/\sqrt{s}\,.$$

Here, it is assumed that FB 1 is the remnant of the incoming hadron a moving in the positive z-direction prior to the interaction, while FB 2 stems from hadron b moving in the opposite direction. On the average the leading FBs carry the largest part of the longitudinal momenta as a consequence of the weighting (9). This forces the other FBs to have accordingly less longitudinal momenta. In this manner the factor $A_{\rm l}^2$ is the equivalent of the structure functions used in refs. [1,2].

The method of calculating the longitudinal phase-space of N FBs is taken from ref. [23] with appropriate modifications due to the presence of $A_{\rm l}^2$.

2.5 Statistics $A_{\rm st}^2$

In conclusion, all factors still necessary for a correct counting of the final states are collected in the term

$$A_{\rm st}^2(\alpha_N) = \left\{ \prod_{I=1}^{N} g(\alpha_I) \left(\frac{V}{(2\pi)^3}\right)^{n_I-1} \left[\prod_{i=1}^{n_I} (2\sigma_i+1) 2m_i\right] \right\} \left(\frac{V}{(2\pi)^3}\right)^{N-1} . \tag{10}$$

It contains the spin degeneracy factors $(2\sigma_i+1)$, the volume V in which the particles are produced with $V = 4\pi R^3/3$ determined by the radius parameter R. The quantity $g(\alpha_{\rm I}) = \left(\prod_\beta n_\beta!\right)^{-1}$ is the degeneracy factor for groups of n_β identical particles in the final state of the I-th FB and prevents multiple counting of identical states.

2.6 Differential cross section

Summarizing the above considerations we define the number of states in the decay channel α_I of one FB

$$\mathrm{d}\mathcal{Z}_I(\alpha_I) = g(\alpha_{\rm I}) \left(\frac{V}{(2\pi)^3}\right)^{n_I-1} \left\{\prod_{i=1}^{n_I} (2\sigma_i+1) 2m_i\right\} \mathrm{d}M_I \left(\frac{M_I}{\Theta}\right) K_1\left(\frac{M_I}{\Theta}\right) \mathrm{d}L_{n_I}(M_I;\alpha_I) \tag{11}$$

and the analogous number for the set of FB states

$$\mathrm{d}\mathcal{Z}_N(s) = \left(\frac{V}{(2\pi)^3}\right)^{N-1} \left\{\prod_{I=1}^{N} 2M_I \exp(-\gamma P_{\rm t,I}) A_{\rm l}^2(N)\right\} (X_1X_2)^{\beta} \mathrm{d}L_N(s;M_1,\ldots,M_N)\,. \tag{12}$$

From eqs. (11) and (12) a compact expression for the probability of populating the channel $\boldsymbol{\alpha}_N = (\alpha_1,\ldots,\alpha_N)$ [see eq. (3)] can be derived

$$\mathrm{d}W(s;\boldsymbol{\alpha}_N) = \left\{\prod_{I=1}^{N} \mathrm{d}\mathcal{Z}_I(\alpha_{\rm I})\right\} \mathrm{d}\mathcal{Z}_N(s)\,. \tag{13}$$

The corresponding cross section is written as

$$\mathrm{d}\sigma(s) = \sigma_{\rm in}(s) \frac{\mathrm{d}W(s;\boldsymbol{\alpha}_N)}{\sum_N \sum_{\boldsymbol{\alpha}_N} \int \mathrm{d}W(s;\boldsymbol{\alpha}_N)}\,, \tag{14}$$

where the inelastic cross section $\sigma_{\rm in}(s)$ of the considered reaction serves as normalization. Any physical quantity of interest can be derived from eq. (14) by summing the contributions from all channels and integrating over the unobserved variables

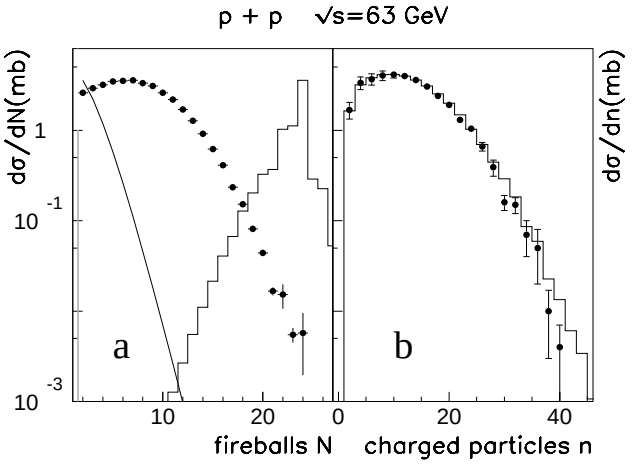

Fig. 2. The calculated FB distribution $\mathrm{d}\sigma/\mathrm{d}N$, eq. (15), (dots in **a**) and the measured [24] and calculated multiplicity distribution $\mathrm{d}\sigma/\mathrm{d}n$ of charged particles n (dots and histogram respectively in **b**) from pp interactions at $\sqrt{s} = 63\,\mathrm{GeV}$. In **a** the dependence of the matrix element $A_\mathrm{i}^2(N)$ (line) and of the FB distribution without $A_\mathrm{i}^2(N)$ (histogram) are depicted separately (these two curves are arbitrarily normalized).

2.7 Adjusting parameters

The parameters introduced in the previous subsections determine definite features of the production process. So the radius parameter is responsible for the multiplicity n of final particles. In eq. (10) the factor V^{n-1} appears implying $R^{3(n-1)}$, and increasing R in turn means that states with large number n of produced particles get higher weights. The temperature Θ and the radius R determine the mean invariant mass of the FBs, Θ via the excitation energy, R via the number of particles in the FB. Abundances of different hadron species are fixed by the probabilities λ_s and λ_c for the creation of the different quark flavors. The parameter Θ_h in eq. (6) influences the selection of hadrons consisting of the same valence quarks. Finally, the momenta of the primary hadrons are composed from the superposition of the FB momenta, determined by β and γ, with the relative velocities of hadrons in the rest frames of the FBs, influenced by Θ. There are correlations between the parameters, and several parameter sets have been found giving similar results.

In searching for a suited set of parameters we start at the highest energy $\sqrt{s} = 63\,\mathrm{GeV}$ with a guess for all parameters except N and D, which are responsible for the number of produced FBs [see eq.(4)]. These parameters are varied until the multiplicity distribution of charged particles is reasonably reproduced.

In fig. 2 the influence of the factor $A_\mathrm{i}^2(N)$ on the FB distribution

$$\frac{\mathrm{d}\sigma(s)}{\mathrm{d}N} = \sigma_\mathrm{in}(s)\frac{\sum_{\boldsymbol{\alpha}_N}\int \mathrm{d}W(s;\boldsymbol{\alpha}_N)}{\sum_N\sum_{\boldsymbol{\alpha}_N}\int \mathrm{d}W(s;\boldsymbol{\alpha}_N)} \qquad (15)$$

is demonstrated. Without the factor $A_\mathrm{i}^2(N)$ the cross section for producing N FBs (the histogram in fig. 2a) reaches its maximum at values much too high for reproducing the multiplicity distribution of charged particles. By combining the increasing phase-space factor with the decreasing function $A_\mathrm{i}^2(N)$ (the line in fig. 2a) a FB distribution is produced which reproduces the distribution of charged particles (fig. 2b). The similarity of FB and particle multiplicity distribution is due to the fact that on the average each FB emits the same number of particles.

In order to describe data also at lower energies the parameters W_v, γ, β and R were made energy dependent, while the other ones are kept constant. For the probability W_v of valence quark removal the energy dependence follows from the consideration of the binary reactions $pp \to n\Delta^{++}$ and $pp \to \Delta^0\Delta^{++}$ for which data in a wide energy region are available (see fig. 3). In the present approach contributions to these reactions come alone from events with $N = 2$ FBs. A removed quark from one proton belongs, after the interaction, to the other one and vice versa. For the reaction to proceed an exchange of an u with a d quark must happen according to

$$p + p \to uud + uud \to udd + uuu \to n + \Delta^{++}\ .$$

The calculated cross sections become zero for $W_\mathrm{v} = 0$, while for $W_\mathrm{v} = 1$ the data are well reproduced at low, but overestimated by orders of magnitude at high energies (see the dashed curves in fig. 3). Therefore, the function

$$1 - W_\mathrm{v} = E_\mathrm{k}/(W_1 + E_\mathrm{k}) \qquad (16)$$

with the excess energy $E_\mathrm{k} = \sqrt{s} - 2m_p$ and one parameter W_1 is used to describe the energy dependence. It provides a smooth transition between the two extremes, $W_\mathrm{v} = 1$ for excess energy $E_\mathrm{k} = 0$ and $W_\mathrm{v} \to 0$ for large excess energies. In this way the data are reproduced quite well with the correspondingly adjusted parameter W_1 (see table 1). Such an energy dependence is in agreement with the

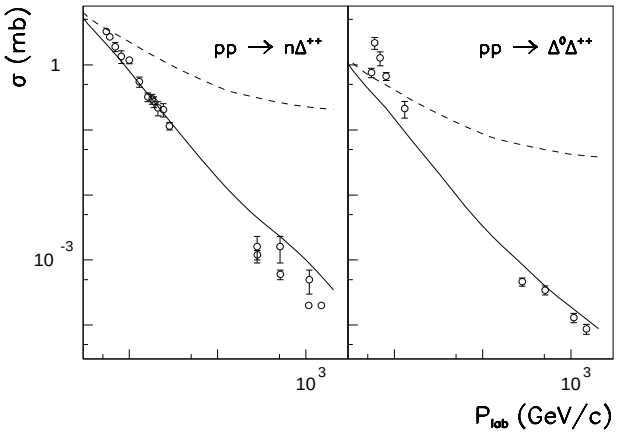

Fig. 3. Cross section of the reactions $pp \to n\Delta^{++}$ and $pp \to \Delta^0\Delta^{++}$ as a function of the laboratory momentum. Experimental data (dots) from [25] are compared with ROC model results (solid lines). The dashed curves are calculated with the probability for valence quark removal $W_\mathrm{v} = 1$.

Table 1. The parameter set used for the calculations. ME stands for the matrix element squared.

ME	Parameter	Parameter	Equation
$A_{\rm i}^2$	$\bar{N}$=1.8	D=1.4	4
$A_{\rm qs}^2$	$\lambda_{\rm s}$=0.15	$\lambda_{\rm c}$=0.05	5
	$\Theta_{\rm h} = 250\,\mathrm{MeV}$	$W_1 = 3\,\mathrm{GeV}$	6,16
$A_{\rm ex}^2 A_{\rm st}^2$	$\Theta = 300\,\mathrm{MeV}$	R=1.2 . . . 1.29 fm	7,10
$A_{\rm t}^2$	$\gamma_0 = 3.8\,(\mathrm{GeV/c})^{-1}$	$\gamma_1 = 1\,\mathrm{GeV}$	8,17
$A_{\rm l}^2$	$\beta_0 = 2$	$\beta_1 = 1\,\mathrm{GeV}$	9,18

parton picture of hadrons. Roughly speaking the number of partons increases with energy and, consequently, the probability for a valence quark being involved in the color exchange diminishes.

The energy dependence of the parameters γ and β [see eqs. (8), (9)] cannot be determined in such a clean way. Still the best indication comes from the proton spectra at different energies. In a diffractive event at least one of the leading FBs is identical with the corresponding initial hadron. The additional folding with the momentum distribution from the FB decay is absent and the transverse momentum dependence of the diffractive peak (see figs. 9 and 10 in sect. 3.2) is directly governed by γ and β. A reasonable description at the different energies is achieved using

$$\gamma = \gamma_0 \sqrt{s}/(\gamma_1 + \sqrt{s}) \tag{17}$$

and

$$\beta = \beta_0 \sqrt{s}/(\beta_1 + \sqrt{s})\,. \tag{18}$$

The parameter R is then adjusted to reproduce the mean multiplicity of charged particles $\langle n_{\rm ch}\rangle$ at the different energies. Below incident momenta of 100 GeV/c the constant value of $R = 1.29\,\mathrm{fm}$ is used, because $\langle n_{\rm ch}\rangle$ ceases to be sensitive to the value of R. With increasing energies the value of R decreases smoothly towards 1.2 fm. All ROC model results in this paper are calculated with the parameter set summarized in table 1.

3 Comparison with data

The ROC model is implemented as a Monte-Carlo generator which samples complete events from which nearly all kinds of measurable quantities can be deduced and compared with experimental results. The overall agreement between data and ROC calculations is quite good in the whole considered energy range between about $\sqrt{s} \approx 2.2\,\mathrm{GeV}$ and the highest ISR energy of $\sqrt{s} = 63\,\mathrm{GeV}$. In the following a few selected data sets concerning hadron multiplicities and the dependencies of differential cross sections on longitudinal and transverse variables are presented. Then correlations are discussed more thoroughly, because they are sensitive to differences between string and FB models.

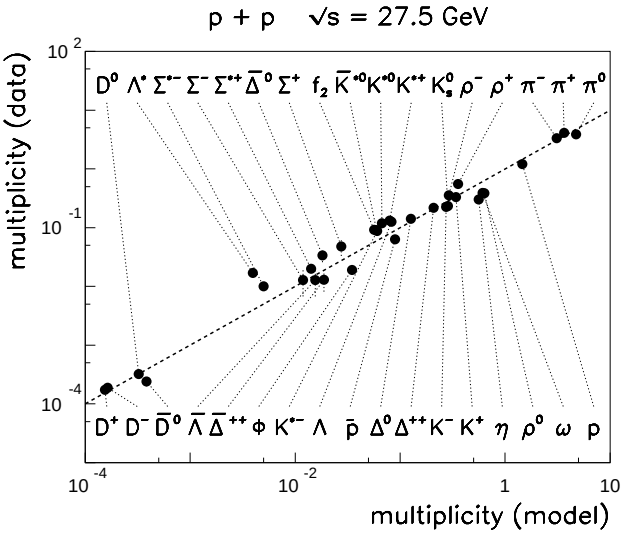

Fig. 4. Hadron multiplicities for *pp* collisions at $\sqrt{s} = 27.5\,\mathrm{GeV}$. The experimental average multiplicities [25,26,27] are plotted versus the calculated ones. The dashed line indicates coincidence between data and calculations. Well reproduced data tend to lie near this line. Λ^* stands for $\Lambda(1520)$.

3.1 Multiplicities

Hadron abundances are determined by the strange and charm suppression factors $\lambda_{\rm s}$ and $\lambda_{\rm c}$, respectively, and the hadron temperature $\Theta_{\rm h}$. There is no parameter which governs the production of baryons directly. Instead, the algorithm for building hadrons from quarks is responsible for baryon production. The more quarks are available in the FB considered, the more probable it is to select at random a sequence of three q's (or $\bar{q}$'s) from which a baryon (or antibaryon) can be formed. Since the FBs become bigger with increasing temperature Θ and radius R, these are the parameters, which determine how many baryons are produced. A rather complete data set of hadron multiplicities for *pp* collisions at $\sqrt{s} = 27.5\,\mathrm{GeV}$ is compared with model calculations in fig. 4. The agreement is quite impressive except for the $\Lambda(1520)$ where the deviation is rather large. An obvious reason for this discrepancy has not been found.

Figure 4 should be compared with the result from the thermodynamical model of Becattini (see fig. 5 in ref. [10]). There, three parameters, temperature, volume and suppression factor $\lambda_{\rm s}$ are fitted, which have similar meanings as in our study, although the parameter values differ considerably from those used here. Nevertheless, the achieved accuracy of the description is comparable. We have, contrary to ref. [10], charmed particles included in fig. 4, and the suppression factor $\lambda_{\rm c}$ is adjusted to reproduce these data points.

In fig. 5 the energy dependence of mean multiplicities of different particle species is plotted. The mean multiplicity of charged particles $\langle n_{\rm ch}\rangle$ is mainly affected by the temperature Θ and the radius R. In order to reproduce $\langle n_{\rm ch}\rangle$ the radius R is adjusted at each energy. The

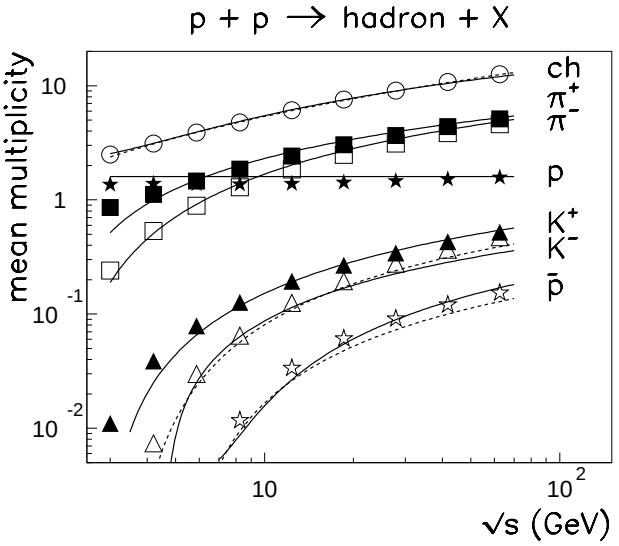

Fig. 5. The energy dependence of mean multiplicities of charged particles (ch), π^+, π^-, K^+, K^-, p and $\bar{p}$ for pp scattering. Full and dotted lines are fits to the data [28], the symbols are ROC results.

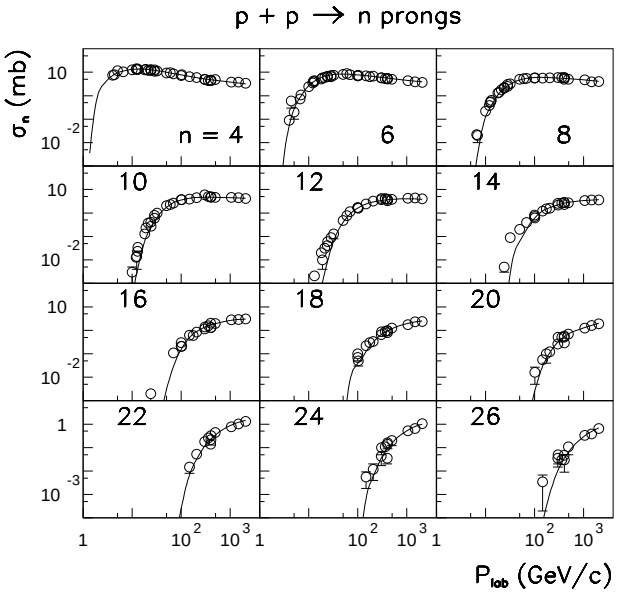

Fig. 6. The topological cross sections σ_n for the production of n charged particles as a function of the laboratory momentum. Dots are data [25], full lines ROC results.

adapted values of R change by less than 10% in the considered energy region. Since charged particles are mainly pions the energy dependences of the number of charged particles and of pions are similar. The slightly larger values of π^+ compared to π^- arise from charge conservation. Strangeness suppression causes a large gap between pions and kaons. It should be noted that, *e.g.*, the VENUS model reproduces this gap (see fig. 10.2 of ref. [2]) with a suppression $u : d : s = 0.43 : 0.43 : 0.14$ differing by a factor of nearly two from the value used here, namely $u : d : s = 1 : 1 : 0.15$. A possible explanation for this difference might be the mass factor in eq. (10). Strange particles have heavier masses what gives them a larger relative weight. On the other hand, the phase-space factor becomes smaller the heavier the produced particles are. Hence, a direct comparison of the suppression factors as used in string fragmentation and in the present approach seems to be difficult. The production of antiprotons is suppressed by about two orders of magnitude, because only FBs consisting of at least three quark pairs have a certain probability to create a baryon-antibaryon pair. The direct influence of the phase-space factor becomes especially important in the threshold region where the multiplicities are small. The different curves for pions, kaons and antiprotons are well reproduced due to the phase-space factor, which strongly decreases with diminishing kinetic energy still available after particle production.

After having reproduced the mean multiplicities of charged particles by adapting the radius parameter we consider the energy dependence of topological cross sections in fig. 6 without any further parameter adjustment. The typical behavior of the cross sections with a weak maximum and subsequent slow decrease for low and a continuous increase in the considered energy region for high multiplicities is well reproduced by our model.

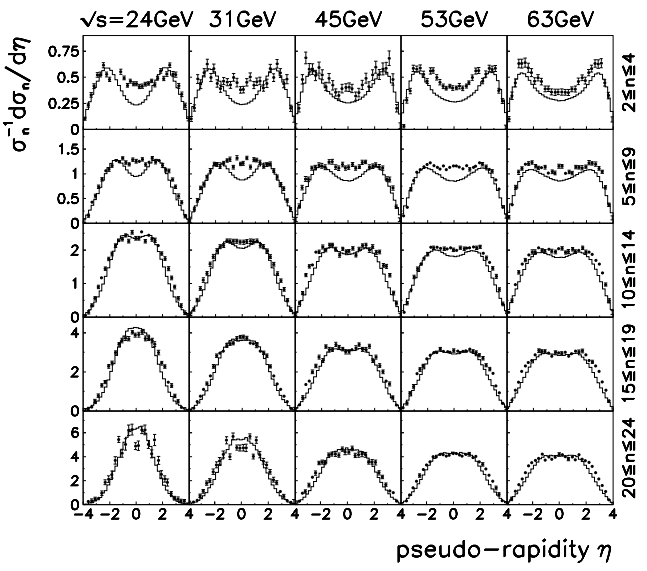

Fig. 7. Normalized charged particle densities in various intervals of the multiplicity n indicated on the right ordinate. Dots are data [29], histograms represent ROC results. Data and calculations are corrected for acceptance. For the data n is the *observed* multiplicity, while for the calculations n is the (true) multiplicity in the pseudo-rapidity range $\eta \leq 4$.

3.2 Differential cross sections

In a next step the distribution of particles in phase-space is considered. We start with the charged particle density for various intervals of the *observed* multiplicity shown in fig. 7. Charged particles were measured [29] in the pseudo-rapidity region $|\eta| \leq 4$. In the calculations the geometrical

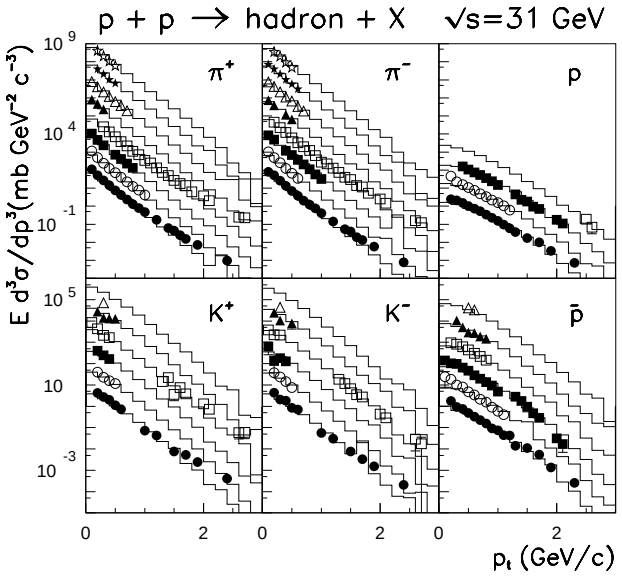

Fig. 8. Invariant cross sections as a function of the transverse momentum at cm. rapidities y=0, 0.2, 0.4, 0.6, 0.8, 1.0, 1.2 and 1.4 from bottom to top. Symbols are data [30], histograms ROC results. The spectra are multiplied by 10^0 at y=0, 10^1 at y=0.2 ... 10^7 at y=1.4.

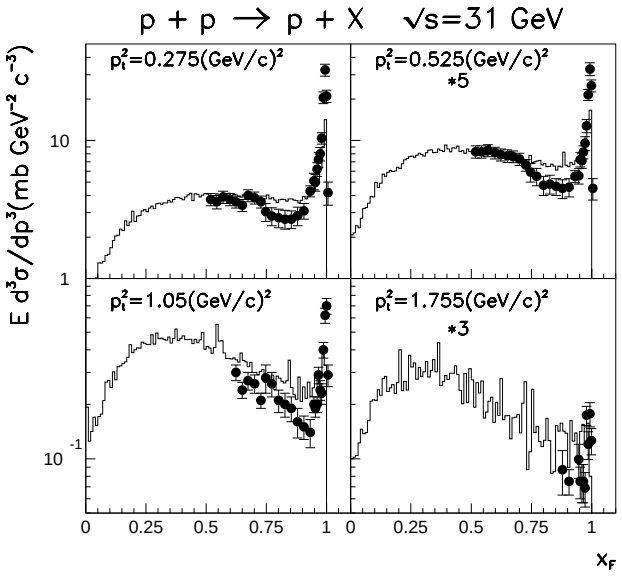

Fig. 9. Invariant differential cross sections as a function of Feynman's variable x_F at various values of p_t^2 as indicated in the figure. Symbols are data [31], histograms ROC results. The spectra on the right hand side are multiplied by factors of 5 and 3, respectively.

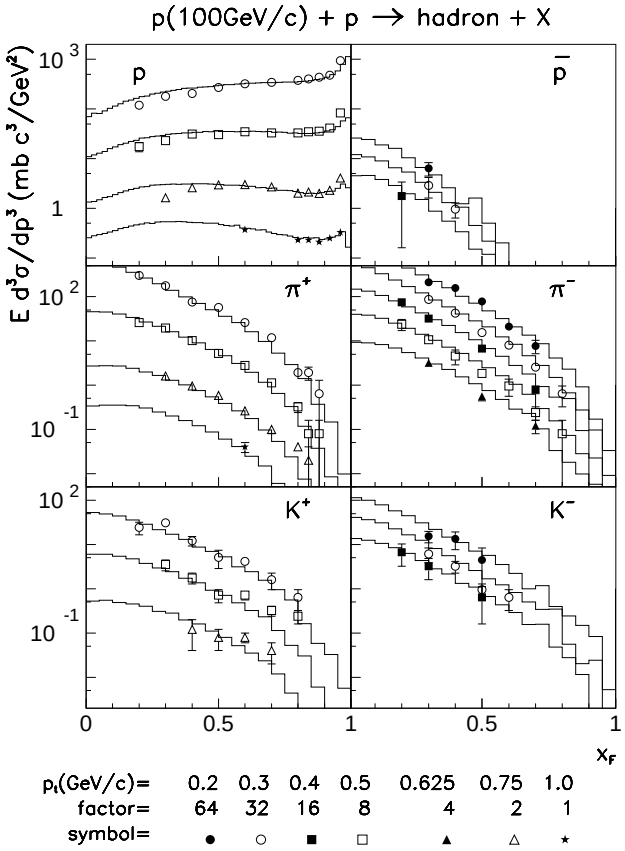

Fig. 10. Invariant differential cross section for the production of $p, \bar{p}, \pi^+, \pi^-, K^+$ and K^- as a function of Feynman's variable x_F. The symbols denote the data [32] at various values of the transverse momentum p_t, histograms are ROC results. Data and calculations are multiplied by the factors given in the legend.

acceptance of the apparatus has been taken into account according to the curve given in fig. 2 of ref. [29]. The differences in the multiplicities *observed* in the experiment and the multiplicities in the calculations are, however, not corrected. Nevertheless, the characteristic features of the data are excellently reproduced. We see the two bump structure at low and the shrinkage of the distributions with increasing multiplicities as well as their broadening with increasing energy. In the ROC calculations this behavior comes from the decay of the leading FBs situated near the projectile and the target rapidity at low multiplicities, while with increasing multiplicity the contributions from the increasing number of FBs dominate and due to momentum conservation the mean rapidity of the leading FBs change to lower values too.

The same data were described by ref. [35] with a simple cluster model and by [36] in the framework of the dual parton model [1]. Both attempts failed in reproducing the two-bump structure at low multiplicities, obviously due to the absence of a diffractive component in these approaches.

In fig. 8 transverse momentum distributions for various particles are compared with experimental data. Both data and model results show roughly an exponential behavior. The calculated spectra result from a convolution of the transverse momenta of the FBs with the internal momentum distributions of the primary particles in the FBs and the momentum distributions of secondaries in which primary resonances decay. At the highest momenta

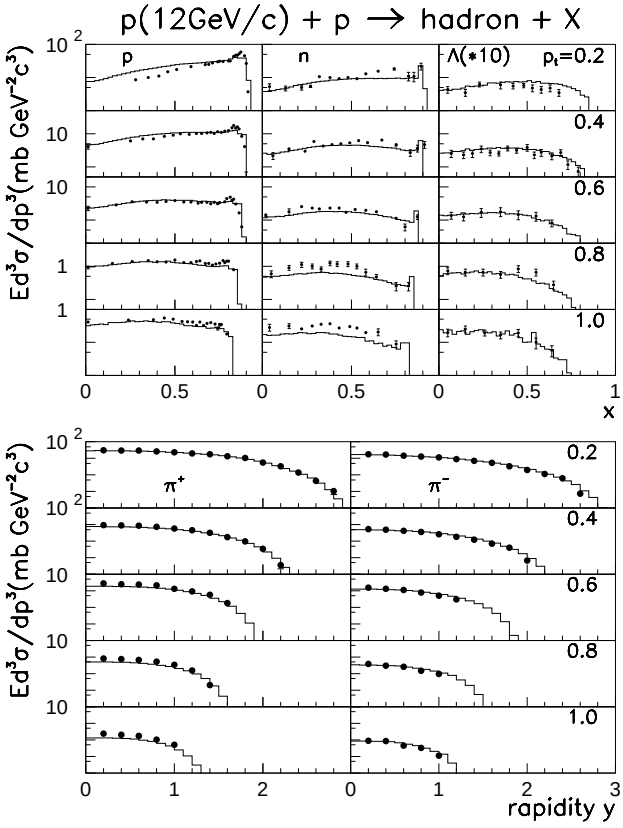

Fig. 11. Invariant differential cross sections for the production of protons, neutrons and Λ's as a function of $x = 2p_l/\sqrt{s}$ (upper part) and of π^+ and π^- mesons as a function of the rapidity y (lower part). The symbols denote the data [33,34] at values of the transverse momentum p_t between 0.2 and 1.0 GeV/c, histograms are ROC results.

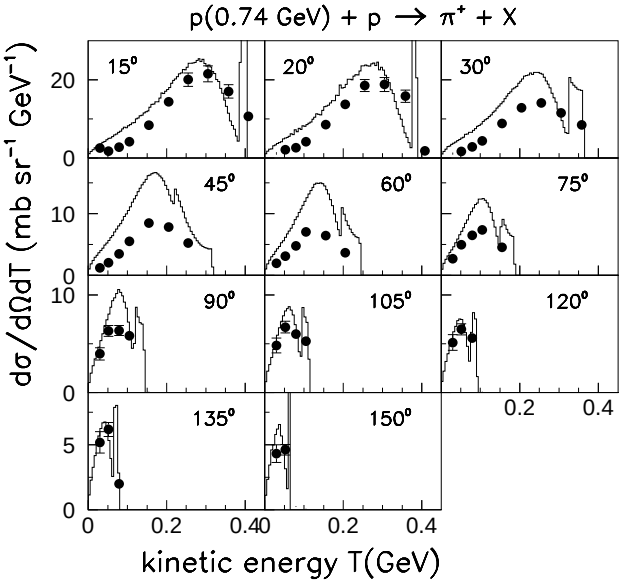

Fig. 12. Differential cross section as a function of the kinetic energy for π^+ production at laboratory angles between 15° and 150°. Dots are data [37], histograms ROC results.

an underestimation of the measured cross section is observed while the overall agreement is quite satisfactory for all particle types.

Proton spectra as a function of a longitudinal variable like Feynman's variable x_F are of special interest because of the peak from diffractive scattering for $x_F \to 1$. As already mentioned there is no special parameter which forces this channel to have a definite probability. Therefore, the good overall reproduction of the proton spectra in fig. 9 is quite remarkable, although the height of the peak is underestimated by the calculations. A better agreement might be obtained by giving the leading FBs a lower temperature than the central ones in analogy to the spectator-participant picture of hadron-nucleus reactions. This ansatz will be left to forthcoming considerations.

Also at lower energies excellent agreement between data and ROC model calculations is achieved, as demonstrated in fig. 10. There the dependence of invariant differential cross sections on Feynman's variable x_F for the production of various hadron species at a laboratory momentum of 100 GeV/c is depicted. While the proton spectra show pronounced diffractive peaks for $x_F \to 1$, the cross sections for the other particle types strongly decrease at large x_F. The squared longitudinal matrix element A_l^2 with the parameter β in eq.(9) governs this behavior. It keeps the leading FBs at large $|x_F|$ and the particles from the central FBs at small $|x_F|$. The smaller β is chosen the larger the cross sections become for mesons and $\bar{p}$'s for $x_F \to 1$.

In stepping down the energy scale let us give a further example in fig. 11. Shown are the invariant cross sections for three types of baryons as a function of $x = 2p_l/\sqrt{s}$ (p_l being the longitudinal momentum) and for charged pions as a function of the rapidity . The main features of the data are well reproduced, although again the diffractive peaks in the proton spectra are underestimated. In case of the neutron spectra there are deviations especially at higher values of p_t, while the Λ spectra are quite well described. Also the rapidity plateau at small and its shortening with increasing transverse momenta in the pion spectra is well reproduced.

Finally, we verify the applicability of the ROC model at energies below the production threshold for strange particles and show the kinetic energy spectra of π^+ mesons at an incidence energy of 740 MeV in fig. 12. The peak at the high-energy end of the calculated spectra comes from the binary reaction $pp \to d\pi^+$. Due to insufficient energy resolution this peak is not seen in the measured spectra. The data are well reproduced in forward and backward direction while deviations become noticeable at sidewards angles. At low energy the parameter values discussed in sect. 2 are no longer important. Instead, the details of the treatment of resonance decays play an important role. Most of the π^+ meson production proceeds via the creation of Δ resonances. The spectra are therefore strongly influenced by the mass distributions of the decayed resonances. In the present version of the ROC model the

current masses of all types of resonances are sampled by using a constant width of the Breit-Wigner distribution. This might be the reason for the observed deviations.

3.3 Correlations

The data considered so far can obviously be quite well reproduced by both string and FB models. In this subsection the question is discussed whether rapidity correlations are more sensitive with respect to their interpretation in terms of strings or FBs. The existence of short-range correlations is experimentally well established and many papers deal with the various aspects of correlations (see, *e.g.*, [38,39, 40,41,42,43]).

When looking for rapidity correlations one usually defines a single-particle

$$\rho_1(y) = \sigma_{\rm in}^{-1} \mathrm{d}\sigma/\mathrm{d}y$$

and a two-particle rapidity density

$$\rho_2(y_1, y_2) = \sigma_{\rm in}^{-1} \mathrm{d}^2\sigma/\mathrm{d}y_1\mathrm{d}y_2.$$

The latter is proportional to the probability of finding one particle at y_1 and a second one at y_2. In order to see whether the joint production of a pair of particles at (y_1, y_2) differs from an independent production of the two particles the two-particle correlation function

$$C(y_1, y_2) = \rho_2(y_1, y_2) - \rho_1(y_1)\rho_1(y_2) \qquad (19)$$

is introduced as the difference between the two-particle density and the product of two single-particle densities. Non-vanishing values of $C(y_1, y_2)$ indicate the presence of correlations.

In fig. 13 the measured and calculated two-particle correlation functions for different charge combinations of the two observed particles are compared. The pronounced peaks in the measured spectra are satisfactorily reproduced by the ROC model calculations (histograms). However, this fact alone is not yet a proof of the existence of FBs for at least two reasons. First, the measurements are inclusive ones and mixing of events with different multiplicities can cause strong correlations as, *e.g.*, pointed out in refs. [40,46,47]. Second, the presence of resonances among the emitted particles also tends to group the observed particles into clusters. That means, the observed correlation spectra contain always a superposition of effects from resonances and other possible short-range phenomena.

In order to see whether resonance production alone can reproduce the observed correlation patterns we carry out calculations with a special version of the ROC model (abbreviated by ROCS in the following). All FBs are compelled to degenerate into single hadrons by restricting the quark content of the FBs to be either qqq or $\bar{q}\bar{q}\bar{q}$ or $q\bar{q}$. In this way all correlations implied by the presence of FBs are excluded. An additional parameter $W_{\rm B}$ is necessary in this case fixing the probability of baryon creation relative

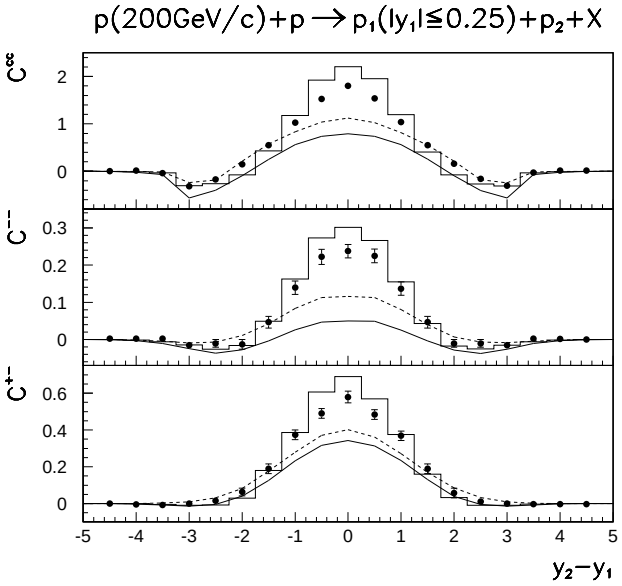

Fig. 13. The inclusive two-particle correlation function $C(y_1, y_2)$ from 200 GeV/c *pp* interactions as a function of $y_2 - y_1$ with fixed $|y_1| \leq 0.25$ for different charge states of the two observed particles indicated by C^{cc}, C^{--} and C^{+-}. Dots are data [44], histograms ROC model, full lines PYTHIA and dashed lines ROCS results.

to meson production, because the algorithm for the combined building of baryons and mesons from quarks (see sect. 2.2) is not applicable here. The value of $W_{\rm B} = 0.15$ adjusted to reproduce $\bar{p}$ production is similar to the probability of diquark creation in string models, where, *e.g.*, the default values used in VENUS [2] and PYTHIA [6] are 0.12 and 0.10, respectively. The ROCS version has been proven to reasonably reproduce most of the data discussed in the previous sections with readjusted parameters of $A_{\rm i}^2$ [see eq. (4)] and an increased radius parameter R. The ROCS results for the correlation are shown in fig. 13 by the dashed lines, which underestimate the measured values remarkably. We consider this result as a direct verification of the presence of short-range phenomena beyond resonance production.

As a further proof of such additional short-range phenomena calculations with the string model PYTHIA [6] version 6.115 are carried out using the multiple interaction approach of ref. [5] with varying impact parameter. The mean multiplicity of charged particles is reproduced by adjusting the regularization scale $p_{\perp 0}$ (PARP(82)) of the transverse momentum spectrum. A Gaussian is taken for the matter distribution of the interacting protons, what gives a reasonable reproduction of the multiplicity distribution of charged particles at $\sqrt{s} = 63$ GeV. All other parameters are kept at their default values. The results, the full lines in fig. 13, underestimate the data too. This finding confirms again that resonance production alone is insufficient for a correct reproduction of correlation data. In addition, the similarity of ROCS and PYTHIA curves shows that the fragmentation of multiple strings in PYTHIA

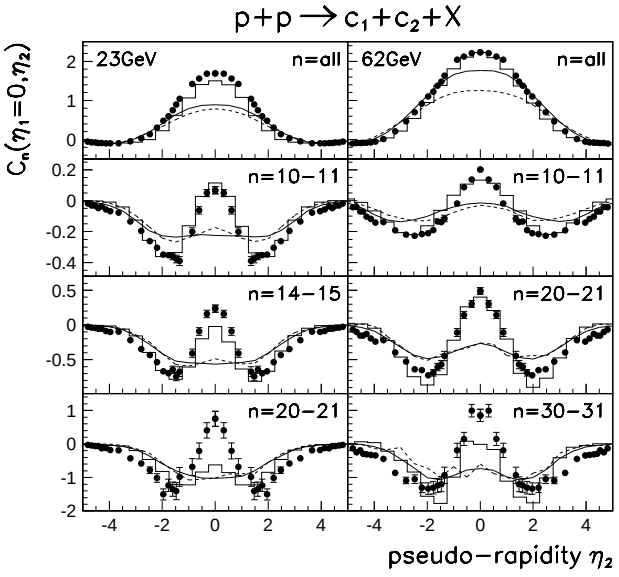

Fig. 14. Inclusive (n=all) and semi-inclusive two-particle correlations $C_n(\eta_1, \eta_2)$ vs. η_2 at fixed $\eta_1 = 0$ for the *observed* multiplicities n indicated in the figure from pp interactions at $\sqrt{s} = 23$ GeV and 62 GeV. At 23 GeV the corresponding mean values of the *true* multiplicities are 9.1, 14.0 and 21.7, and the curves are calculated for multiplicities of 8-10, 14 and 18-24, respectively, while at 62 GeV the mean values are 8.1, 18.8 and 30.8, and the curves are calculated for multiplicities of 8, 18-20 and 28-34, respectively. Dots are data [45], histograms ROC model, full lines PYTHIA and dashed lines ROCS results.

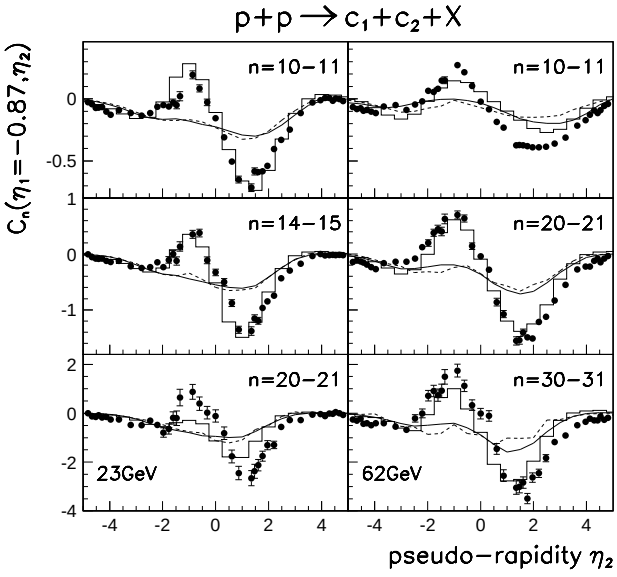

Fig. 15. The same as fig. 14, but for semi-inclusive two-particle correlations $C_n(\eta_1, \eta_2)$ vs. η_2 at fixed $\eta_1 = -0.87$.

can be quite well imitated by creating hadrons in longitudinal phase-space.

Correlations caused by the mixing of events with different multiplicities can be excluded by fixing the multiplicities of the considered events. This type of measurements will be called semi-inclusive in the following. For the correlation function the same formula (19) holds with the single and two-particle densities taken from events having a definite multiplicity. As an example results of Amendolia *et al.* [45] are presented in fig. 14 for the reaction $p + p \to c_1 + c_2 + X$ at two energies with c_1, c_2 and X standing for two charged particles and anything, respectively. The inclusive two-particle correlation (on top of the figure) is compared with semi-inclusive correlations at three narrow intervals of the *observed* multiplicities. The latter data sets, however, contain events whose *true* multiplicities span a much wider interval (see fig. 5 in ref. [45]). Lacking the exact knowledge of the detector response we have selected multiplicity intervals around the mean values of the *true* multiplicities [45] in the calculations. Figure 14 shows that the inclusive correlation function is much broader than the semi-inclusive ones, a feature of the data which is well reproduced by the ROC calculations. The semi-inclusive data with their distinctly smaller peaks and and pronounced dips of both sides of the peaks are well described too. Alone the peaks in the data for the highest multiplicity especially at $\sqrt{s} = 23$ GeV are underestimated. The PYTHIA and ROCS curves clearly underestimate inclusive as well as semi-inclusive data. Again they are in good agreement with each other.

In fig. 15 the correlation function with one charged particle fixed outside midrapidity is given. The data are well reproduced by the ROC model, except for the highest multiplicity interval at $\sqrt{s} = 23$ GeV. These deviations become larger if the distance of the fixed particle from midrapidity is increased (see fig. 16). The ROCS version underestimates also in the non-symmetric cases all considered correlations and agrees with the PYTHIA results with the exception of the lowest multiplicity interval at $\sqrt{s} = 62$ GeV. There, the PYTHIA curve is closer to the experiment than the ROCS result, but still far from a good reproduction of the data.

To better understand the results shown in figs. 14 - 16 the contributions from different subprocesses are depicted in fig. 17 separately. In PYTHIA diffractive and nondiffractive processes are treated in different ways, while in the ROC model a diffractive process is simply one of the possible final channels without any special assumptions. Consequently, the ROC results for all subprocesses exhibit the typical correlation pattern. On the other hand, the PYTHIA results show a large variety of completely different correlation functions in dependence on the considered subprocess and on the pseudo-rapidity interval where one of the particles is fixed. In the first row of fig. 17 the diffractive excitation of the projectile is considered. We find the target proton after the interaction at negative rapidities and the excited projectile as a string in case of PYTHIA and as a number of FBs in case of ROC calculations mainly at positive rapidities. Values of the correlation function around zero near the target rapidity indicate that the emission of the target proton is weakly correlated with the emission of the charged particles from the excited subsystem(s) (see the symmetric

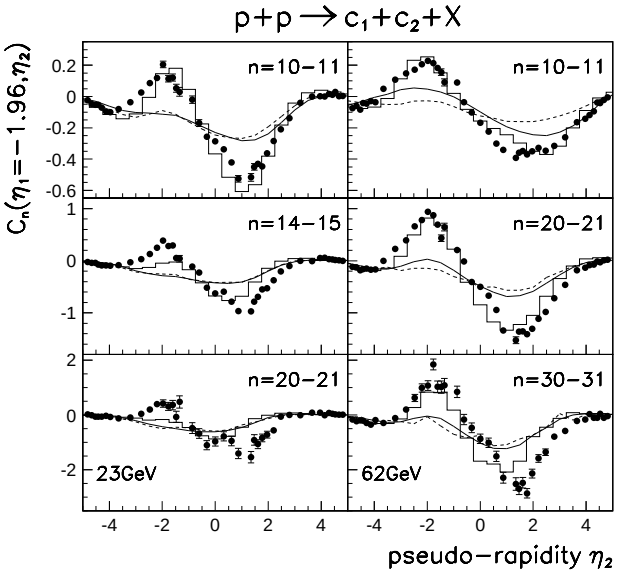

Fig. 16. The same as fig. 14, but for semi-inclusive two-particle correlations $C_n(\eta_1, \eta_2)$ vs. η_2 at fixed $\eta_1 = -1.96$.

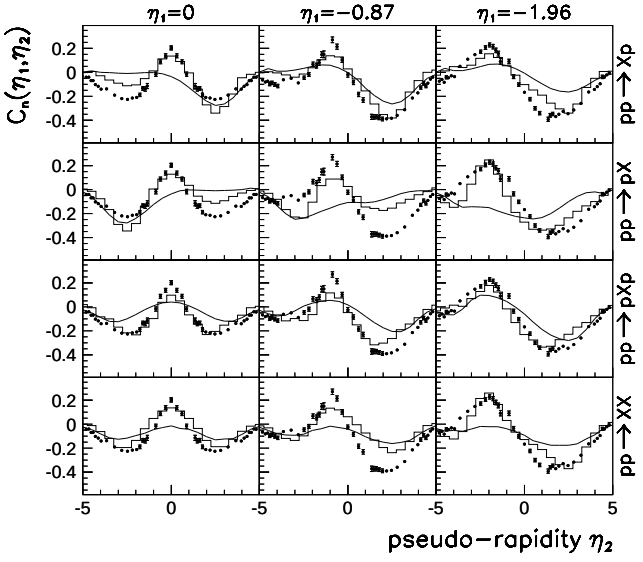

Fig. 17. Semi-inclusive two-particle correlations $C_n(\eta_1, \eta_2)$ vs. η_2 at several fixed values of η_1 indicated in the figure for the multiplicity interval $n = 10 - 11$ at $\sqrt{s} = 62\,\mathrm{GeV}$. The data [45] (dots) are compared with ROC model (histograms) and PYTHIA (full lines) results for single- ($pp \to Xp$ and $pp \to pX$), double- ($pp \to pXp$) and nondiffractive ($pp \to XX$) processes.

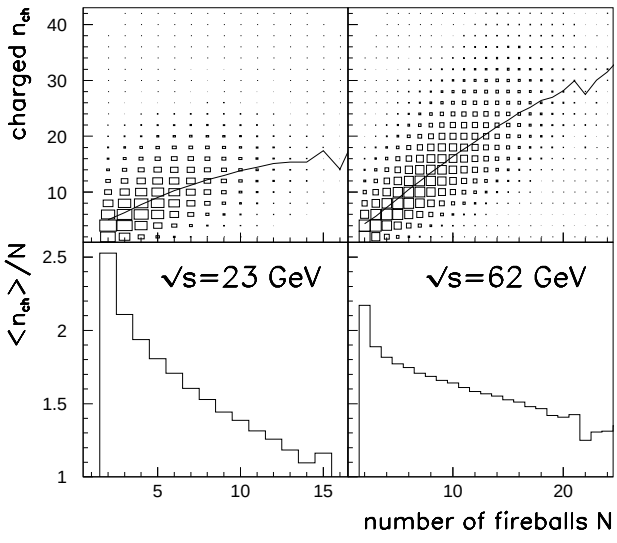

Fig. 18. Number of charged particles n_{ch} versus number of FBs N in ROC model calculations for p+p at $\sqrt{s} = 23\,\mathrm{GeV}$ and 62 GeV. The size of the boxes is proportional to the calculated cross section. The full line in the upper part represents the mean value of charged particles $\langle n_{\mathrm{ch}} \rangle$ and the line in the lower part the FB size $\langle n_{\mathrm{ch}} \rangle / N$ as a function of N.

case $\eta_1 = 0$). For the diffractive excitation of the target (the second row) the unchanged target proton is at positive, the excited subsystems at negative rapidities. The whole picture is simply reversed in the symmetric case ($\eta_1 = 0$), while we get from PYTHIA completely different pictures for the non-symmetric measurements with $\eta_1 = -0.87$ and $\eta_1 = -1.96$. The PYTHIA result for double diffraction (the third row) is of special interest. Both interaction partners remain unchanged and the excited subsystem is mainly at central rapidities. The central string acts like a cluster or FB and the results from ROC and PYTHIA are similar. The contribution of this special process is responsible for the somewhat better reproduction of the data by PYTHIA in the multiplicity interval $n = 10 - 11$ at $\sqrt{s} = 62\,\mathrm{GeV}$ in fig. 16. With increasing multiplicities the diffractive contributions become smaller and the result is dominated by the nondiffractive component. In this case (the fourth row) we have in PYTHIA the typical multi-string picture with a clear underestimation of the measured correlation. Altogether we see that even at fixed multiplicities the contributions from different processes may result in distinct diffraction patterns in a model dependent way.

In spite of the results presented here it should be mentioned that in the literature examples for the description of short-range correlations by string models can be found. So the dual parton model [1], which has a multi-string structure similar to PYTHIA, reproduces correlation data either under certain assumptions for the fragmentation functions (see, *e.g.*, [48,49]) or as the result of the decay of minijets and of soft strings with sea quarks at their ends [50]. Such strings emit hadrons into limited rapidity regions like clusters.

In order to clarify the origin of the deviations between ROC calculations and data at high multiplicities (see fig. 16) we show the correlation between the number of FBs and the number of charged particles in fig. 18. First of all we observe large fluctuations regarding the FB

size, where FB size is understood as the mean number of charged particles originating in a FB. At $\sqrt{s} = 62\,\mathrm{GeV}$ it is possible that, *e.g.*, 18 charged particles may be produced in events with numbers of FBs ranging from 2 up to 20. The mean number of charged particles (the line in the upper part of fig. 18) flattens out for large numbers of FBs especially at $\sqrt{s} = 23\,\mathrm{GeV}$. That means that, although we use constant parameters Θ and R, the FB size (the histogram in the lower part of fig. 18) becomes smaller with increasing number of FBs due to the phase-space factor, and this influence is at $\sqrt{s} = 23\,\mathrm{GeV}$ much stronger than at 62 GeV. Here we see the origin for the discrepancy with the data at high multiplicities. This is confirmed by a series of calculations with increased parameter values of R (and accordingly adapted A_i^2, eq. (4), to keep the mean number of charged particles constant). Due to the larger R the size of the FBs is increased and a good reproduction of the data at high multiplicities is possible while the low-multiplicity data are overestimated. That means, the present version of the ROC model is too simple with regard to the FB size. The volume V derived from the parameter R is considered as a measure for the overlap region of the two colliding hadrons which defines the spatial region where particle production takes place. Therefore, it is understandable that a value of V independent of the impact parameter is surely an oversimplification. Since the number of produced FBs is correlated with the impact parameter (see sect. 2.1), an increase of R with increasing number of FBs would be quite a natural improvement of the model. A dependence of the FB temperature Θ and of the momentum distribution of FBs described by β and γ on the number of FBs cannot be excluded as well. A central collision may produce hotter FBs with a more isotropic phase-space distribution than a peripheral one. Such a view is supported by an analysis [51] of long-range correlations between charged particles emitted into the forward and backward hemispheres at much higher energies ($\sqrt{s} = 0.3 - 1.8\,\mathrm{TeV}$). The E735 collaboration came to the conclusion, that the cluster size may increase as a function not only of $\sqrt{s}$ but also of the particle multiplicity.

An analysis of long-rang correlations in the energy region considered here has been carried out by Uhlig *et al.* [35]. Their results are shown in fig. 19. The mean number of charged particles emitted into the backward hemisphere is plotted as a function of the number of forward emitted particles. The slope of these curves is a measure for the strength of the correlation between particles ejected into the various regions of the hemispheres. Although there are some systematic deviations at low multiplicities and at $\sqrt{s} = 24\,\mathrm{GeV}$ the overall trend of the data is well described by the calculations. We see the strongest correlation for adjacent regions in pseudo-rapidity η while the strength is smaller if there is a gap between the considered η intervals. The emission is nearly independent for the regions in the lowest row of fig. 19, which are outside the central rapidity plateau. The authors of ref. [35] explain their results with the correlation between clusters consisting of about three particles (neutral ones included). In fig. 19

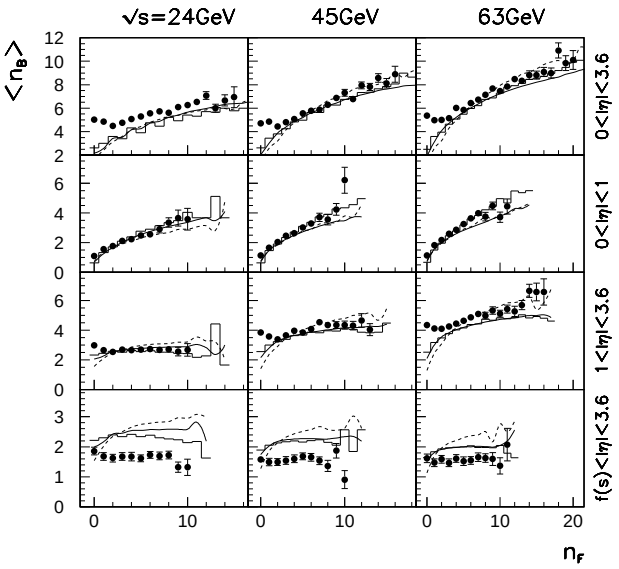

Fig. 19. Mean number of charged particles emitted into the backward hemisphere $\langle n_B \rangle$ as a function of the number of charged particles emitted into the forward hemisphere n_F for symmetric intervals of the pseudo-rapidity η indicated in the figure, where $f(s) = 0.5 \cdot \ln(s \cdot \mathrm{GeV}^{-2}) - 2$. Dots are data [35], histograms ROC model, full lines PYTHIA and dashed lines ROCS results.

we see a striking agreement between the results of ROC, ROCS and PHYTHIA calculations. Obviously, both FB as well as string models are able to reproduce the observed long-range correlations in the considered energy region.

4 Conclusions

We have presented the empirical ROC model for soft hadron production. It is based on the parton picture of hadrons as well as on statistical and thermodynamical considerations. Experimental results from *pp* interactions in the energy region between particle production thresholds and ISR energies can be well described with a moderate number of parameters which are either constant or have a smooth energy dependence. A comparison of the ROC fireball model and the PYTHIA string model with regard to short-range rapidity correlations seems to favor the ROC model, although the description of short-range correlations is possible in string models too. Thus we do not have a clear answer to the problem of hadron production via strings or fireballs. A systematic consideration of all available data especially those at higher energies is necessary to come to a decision between the possible scenarios: strings, fireballs or something in between.

The author would like to thank B. Kämpfer and especially H.-W. Barz for valuable discussions and the careful reading of the manuscript. The work is supported in part by BMBF grants 06DR920 and 06DR828/I.

References

1. A. Capella et al., Phys. Rep. **236**, 225 (1994).
2. K. Werner, Phys. Rep. **232**, 87 (1993).
3. B. Andersson et al., Phys. Rep. **97**, 31 (1983).
4. B. Andersson, G. Gustafson and B. Nilsson-Almqvist, Nucl. Phys. B **281**, 289 (1987).
5. T. Sjöstrand and M. van Zijl, Phys. Rev. D **36**, 2019 (1987).
6. T. Sjöstrand, Comput. Phys. Commun. **82**, 74 (1994).
7. E. L. Feinberg, Usp. Fiz. Nauk **104**, 539 (1971).
8. I. M. Dremin and C. Quigg, Science **199**, 937 (1978).
9. E. L. Feinberg, Usp. Fiz. Nauk **139**, 3 (1983).
10. F. Becattini and U. Heinz, Z. Phys. C **76**, 269 (1997).
11. H. Müller, Z. Phys. A **353**, 103 (1995).
12. H. Müller, Z. Phys. A **336**, 103 (1990).
13. H. Müller, Z. Phys. A **339**, 409 (1991).
14. H. Müller and K. Sistemich, Z. Phys. A **344**, 197 (1992).
15. H. Müller, Z. Phys. A **353**, 237 (1995).
16. H. Müller, Z. Phys. A **355**, 223 (1996).
17. H. Müller, Acta Physica Polonica B **27**, 3385 (1996).
18. E. Fermi, Progr. Theor. Phys. **5**, 570 (1950).
19. E. Byckling and K. Kajantie, *Particle Kinematics* (John Wiley and Sons, London, New York, Sydney, Toronto, 1973).
20. V. Gribov, Sov. Phys. JETP **26**, 414 (1968).
21. V. V. Anisovich and V. M. Shekhter, Nucl. Phys. B **55**, 455 (1973).
22. C. Caso et al., Eur. Phys. J. C **3**, 1 (1998).
23. D. C. Carey and D. Drijard, J. Comput. Phys. **28**, 327 (1978).
24. A. Breakstone et al., Phys. Rev. D **30**, 528 (1984).
25. A. Baldini et al., *Total Cross-Sections for Reactions of High Energy Particles*, vol. 12 of *Zahlenwerte und Funktionen aus Naturwissenschaft und Technik* (Springer-Verlag, Berlin, Heidelberg, New York, London, Paris, Tokyo, 1988).
26. M. Aguilar-Benitez et al., Z. Phys. C **50**, 405 (1991).
27. H. Kichimi et al., Phys. Rev. D **20**, 37 (1979).
28. A. Rossi et al., Nucl. Phys. B **84**, 269 (1975).
29. W. Thomé et al., Nucl. Phys. B **129**, 365 (1977).
30. B. Alper et al., Nucl. Phys. B **100**, 237 (1975).
31. M. Albrow et al., Nucl. Phys. B **54**, 6 (1973).
32. A. E. Brenner et al., Phys. Rev. D **26**, 1497 (1982).
33. V. Blobel et al., Nucl. Phys. B **69**, 454 (1974).
34. V. Blobel et al., Nucl. Phys. B **135**, 379 (1978).
35. S. Uhlig et al., Nucl. Phys. B **132**, 15 (1978).
36. V. Girija and H. Hüfner, Phys. Lett. B **212**, 501 (1988).
37. D. R. F. Cochran et al., Phys. Rev. D **6**, 3085 (1972).
38. A. Basetto, M. Toller and L. Sertorio, Nucl. Phys. B **34**, 1 (1971).
39. F. Hayot, F. Henyey and M. Lebellac, Nucl. Phys. B **80**, 77 (1974).
40. A. Morel and G. Plaut, Nucl. Phys. B **78**, 541 (1974).
41. E. L. Berger, Nucl. Phys. B **85**, 61 (1975).
42. J. Meunier and G. Plaut, Nucl. Phys. B **87**, 74 (1975).
43. J. Benecke and J. Kühn, Nucl. Phys. B **140**, 179 (1978).
44. J. Whitmore, Phys. Rep. **27**, 187 (1976).
45. S. Amendolia et al., Nuovo Cimento A **31**, 17 (1976).
46. K. Eggert et al., Nucl. Phys. B **86**, 201 (1975).
47. R. Ansorge et al., Z. Phys. C **37**, 191 (1988).
48. C. Pajares and A. Varias, Z. Phys. C **19**, 69 (1983).
49. V. M. Chudakov and V. V. Lugovoi, Z. Phys. C **59**, 511 (1993).
50. F. W. Bopp et al., Z. Phys. C **51**, 99 (1991).
51. T. Alexopoulos et al., Phys. Lett. B **353**, 155 (1995).